Chapter 3
Structure-Controlled Synthesis

Abstract Advances in nanoscience and nanotechnology critically depend on the development of nanostructures whose properties are controlled during synthesis. The ability to control and modulate the composition, doping, crystal structure and morphology of semiconductor NWs allows researchers to explore applications of NWs for investigating fundamental scientific questions through developing new technologies. The chapter expands significantly upon the basic methods introduced in the previous chapter for NW synthesis by focusing on controlled growth of a host of NWs with modulated morphologies and structures, including axial and radial heterostructures, kinked, branched, and/or modulated doped structures, where the increased complexity in the NWs can enable unique functional properties.

3.1 Introduction

The capability of creating new nanomaterials and assemblies, with tunable composition and structure on many length scales, offers a driving force towards the scientific breakthroughs that enable revolutionary advances and future technologies. In this regard, one-dimensional (1D) semiconductor NWs serve as one of the most powerful platforms available today in nanoscience, given that it is now possible to rationally design and synthetically realize these structures [1]. These capabilities, unique among different NWs, allow for creating systems or building blocks with predictable physical properties and enable testing fundamental limits of performance. With these characteristics and capabilities, it is also possible to assemble hybrid or multi-component functional architectures using these diverse NW building blocks, leading to rational exploration of possible applications. In this chapter, we summarize the synthesis of five distinct NW structural classes: homogeneous NWs, axial modulated NW structures, radial/coaxial modulated NW structures, branched/tree-like NWs, and kinked NW structures.

A. Zhang et al., *Nanowires*, NanoScience and Technology,
DOI 10.1007/978-3-319-41981-7_3

3.2 Homogeneous Nanowires

Previously in Chap. 2, we have described different synthetic methods to generate homogeneous NWs. In this section, we will discuss diameter-, length-, and doping-controlled synthesis of NWs in more detail.

Central to the nanocluster catalyzed VLS approach to NW growth is the idea that the size of the metal catalysts determine NW diameter, and thus NWs with a narrow size distribution should be obtained from approximately monodisperse nanocluster catalysts. This important idea has been verified through the demonstration of diameter-controlled growth of GaP [2], InP [3], and Si NWs [4] from nearly monodisperse Au nanocluster catalysts. Significantly, the widths of the NW diameter distributions observed in these studies were essentially the same as those of the starting Au nanoclusters, thus demonstrating that NW diameter can be controlled predictably by the nanocluster catalyst.

Pushing the limits of nanocluster catalyst size-controlled growth, Wu et al. [5] described in 2004 the controlled growth of single-crystal SiNWs with diameters approaching molecular dimensions ($\sim$3 nm), exhibiting the smallest diameter SiNWs obtained via VLS process. The cross-sectional high-resolution TEM (HRTEM) images of a representative 3.6-nm SiNW with a $\langle 110 \rangle$ growth axis revealed that the NW had a hexagonal cross section with well-developed facets (Fig. 3.1a–d). Analysis of the lattice-resolved image showed that these facets corresponded to the low-free-energy (111) and (100) planes, consistent with the equilibrium shape (Fig. 3.1d).

Factors affecting the length limits have also been explored in several studies [6–8]. Ultra-long (up to several millimeters) NWs with controlled electronic and/or optical properties could be beneficial for device integration by facilitating the interconnection of individual NWs and NW arrays. Several techniques such as the high-temperature thermal evaporation of silicon monoxide [6] and silicon powders [7] have previously been reported for obtaining millimeter-long SiNWs. However, this goal was still challenging for the nanocluster catalyzed VLS-growth method, as most of the growth rates reported were predominantly in the order of 1–2 μm per minute [9–11]. In the case of SiNWs, the growth rate is strongly temperature-dependent [11, 12], suggesting that the kinetics of thermal decomposition of SiH_4 into atomic Si species could be the rate-determining step and much more important than gas-phase mass transport. Thus, accelerating the decomposition step can significantly enhance the overall growth rate. Due to the lower activation energy for cleavage of Si–Si versus Si–H bonds, disilane (Si_2H_6) was selected as the Si gas precursor for a higher catalytic decomposition rate [8]. Notably, the average SiNW growth rate using Si_2H_6 at 400 °C was 31 μm/min, while the growth rate determined for SiH_4 reactant under similar growth conditions was 130 times lower. Thus, the growth rate of SiNWs can be enhanced by almost 2 orders of magnitude, leading to ultra-high aspect ratio SiNWs, with tens of nanometers in diameter and $\sim$ 2 mm in length (Fig. 3.1e–g).

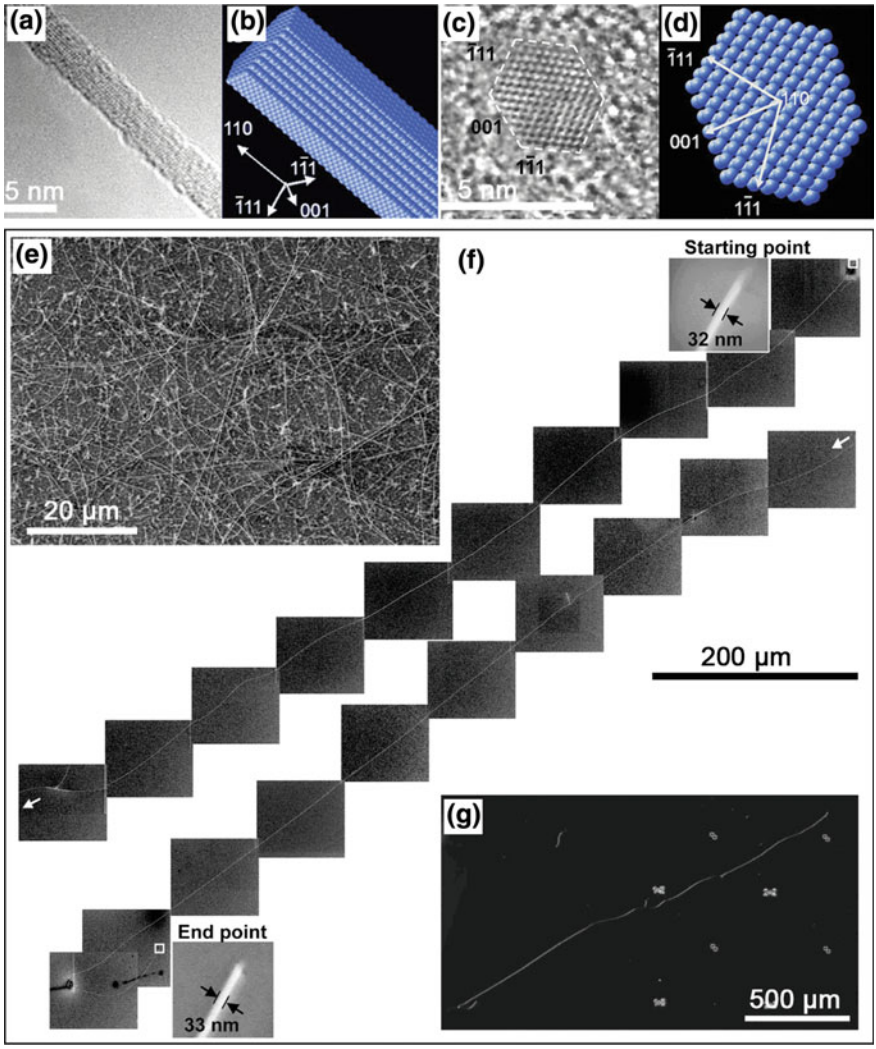

Fig. 3.1 **a** TEM images of 3.6-nm SiNWs grown along the ⟨110⟩ direction, **c** HRTEM cross-sectional image, and equilibrium shapes for the **b** NW and the **d** NW cross sections predicted by Wulff construction. Reproduced from [5]. Copyright 2004 American Chemical Society. **e** SEM image of as-grown ultra-long SiNWs. **f** A series of 20 SEM images of a 2.3 mm long SiNW transferred onto a SiO_2/Si substrate. Insets are SEM images of the starting and end segments of this NW. **g** Dark-field optical image of the same wire. Reproduced from [8]. Copyright 2008 American Chemical Society

In addition to diameter, morphology and length control, doping of NWs is crucial for tuning their physical and chemical properties. In one of the first demonstrations of controlled doping, Cui et al. [13] in 2000 reported LCG-based VLS method to introduce controllably either boron or phosphorus dopants during the vapor phase growth of SiNWs. However, the observed electron mobility values were much lower than expected for *n*-type silicon. Later, substantial efforts focused on studies of hole-doped (*p*-type) SiNWs, while electron-doped (*n*-type) received relatively less attention, although the intrinsic electron mobility in bulk silicon is substantially larger than the intrinsic hole mobility. In 2004, Zheng et al. [10] reported the first example of controlled growth and phosphorus doping of SiNWs, and the fabrication of high-performance *n*-type field effect transistors (FETs) from these nanomaterials.

3.3 Axial Modulated Structures

Modulated nanostructures in which the composition and/or doping are varied on the nanometer scale represent important targets of synthesis, since they can enable new and unique function and potential for integration in functional nanosystems. In this section, we will describe the synthesis of longitudinal NW heterostructures, including semiconductor superlattices, metal-semiconductor junctions, modulation-doped NWs, as well as NWs with ultra-short morphology features. Several reviews focused on semiconductor NW heterostructures have appeared [14, 15].

3.3.1 Early Work

Silicon whiskers with modulated doping concentration were made in the pioneering studies of Wagner for the purposes of elucidating the VLS growth mechanism in 1970 [16]. In 1992, Haraguchi et al. [17] made substantial progress on the growth of GaAs whiskers, including the fabrication of *p*–*n* junctions within whiskers. They employed gold catalyst particles in a reduced-pressure metal-organic chemical vapor deposition (MOCVD) reactor with trimethylgallium ($Ga(CH_3)_3$) and arsine (AsH_3) as precursors to produce cone-shaped nanostructures of micron lengths and ca. 100 nm average diameters. Later, Hu et al. [18] reported two approaches to prepare metal-semiconductor junctions between carbon nanotubes (CNTs) and SiNWs using either a common Fe-based nanocluster catalyst to grow CNTs from the ends of SiNWs or growth of SiNWs from gold clusters electrodeposited onto the CNT free ends.

3.3.2 Semiconductor Heterojunctions

In 2002, a significant step in the controlled synthesis of NW heterostructures was demonstrated by three groups almost simultaneously, with the growth of NW superlattices in a number of systems [19]. Wu et al. [20] combined thermal CVD using $SiCl_4$ with the laser ablation of a solid germanium target to produce Si/SiGe NWs. During the growth process, when the laser was turned on, Ge vapor was generated and both Ge and Si species were deposited into the alloy droplets. The SiGe alloy then precipitated from the solid/liquid interface. By periodically turning the laser on and off, Si/SiGe superlattices were created on every individual NW in a block-by-block fashion. In addition, Björk et al. [21–23] used nanocluster catalysts and MBE techniques to prepare modulated InAs/InP NW structures with periods ranging from 100 to just several nanometers. Significantly, their lattice-resolved TEM images suggested that the interfaces were atomically perfect.

Using a nanocluster catalyzed CVD method, Gudiksen et al. [24] successfully synthesized GaAs/GaP, *n*-Si/*p*-Si, and *n*-InP/*p*-InP axial NW heterostructures and superlattices. As shown in Fig. 3.2a, to create a single junction within the NW, the addition of the first reactant was stopped during growth, and then a second reactant was introduced for the remainder of the synthesis; repeated modulation of the reactants during growth produces NW superlattices. In principle, this approach can be successfully implemented if a nanocluster catalyst suitable for growth of the different superlattice components under similar conditions is used. Figure 3.2b shows a TEM image of a typical GaAs/GaP junction region. Local elemental mapping of the heterojunction by energy dispersive X-ray spectroscopy (EDS) was carried out to probe composition variations across the heterostructure junction (Fig. 3.2c–f). The elemental mapping shows that Ga is uniformly distributed along the length of the NW, while P (Fig. 3.2e) and As (Fig. 3.2f) appear to be localized in the GaP and GaAs portions of the NW heterostructure, respectively. However, quantitative analysis of the P and As composition variations (Fig. 3.2g) show that the junction is not atomically abrupt, but has a transition segment between GaP and GaAs phases over a length scale of 15–20 nm. This length scale is consistent with the expectation that the $\sim$20 nm Au catalyst must re-alloy with GaP after initial GaAs growth. By repeating the modulation process, NW superlattices are produced, in which the number of periods and repeat spacing are readily varied during growth. In this work, a 21-layer GaAs/GaP superlattice was demonstrated, with arbitrary repeat spacing and the segment lengths controlled by the number of pulses delivered to each target.

3.3.3 Metal-Semiconductor Heterostructures

Besides semiconductor heterostructures, metal-semiconductor axial heterostructures and superlattices have also been demonstrated using various methods [25–27]. For

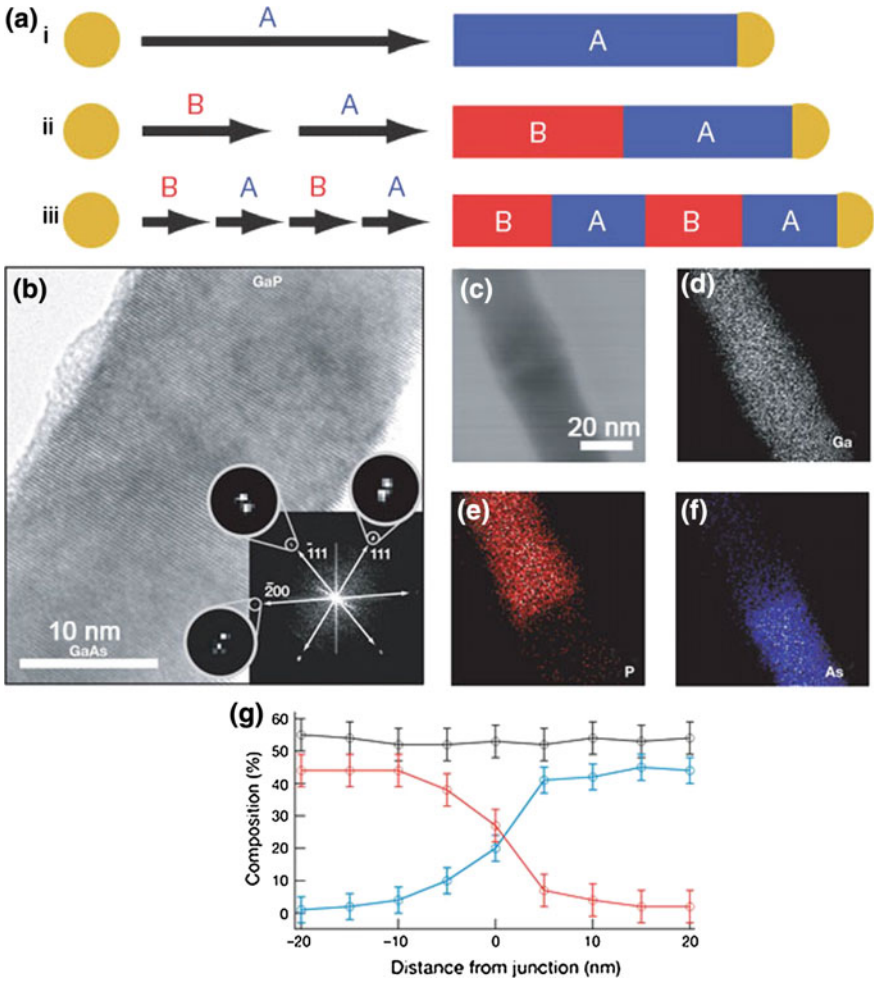

Fig. 3.2 **a** Synthesis of NW superlattices: *i* A nanocluster catalyst nucleates and directs one-dimensional semiconductor NW growth with the catalyst remaining at the terminus of the NW; *ii* upon completion of the first growth step, a different material can be grown from the end of the NW; *iii* repetition of steps *i* and *ii* leads to a compositional superlattice within a single NW. **b**, **c** HRTEM of a GaAs/GaP junction. **d**–**f** Elemental mapping of the Ga (shown *grey*), P (*red*) and As (*blue*) content of the junction shown in **c**. **g** Line profiles of the composition through the junction region. Ga *black*, P *red* and As *blue*. Reproduced from [24]. Copyright 2002 Nature Publishing Group

example, Pena et al. [25] directly synthesized Au/CdSe/Au and Ni/CdSe/Ni segmented NWs by the template method through sequential deposition of materials in polycarbonate membranes, using commercially available plating solutions for Au and Ni segments and acid solution of $CdSO_4$ and SeO_2 for deposition of the semiconducting CdSe segments.

In contrast to direct synthesis, Wu et al. [26] reported that NiSi, a metal, could be obtained from Si via solid phase reaction with Ni. As a result, metallic NiSi NWs were produced by first evaporating Ni on SiNWs, followed by heating the sample above the NiSi transition temperature (Fig. 3.3a). A dark-field optical image of a NiSi/Si NW patterned in this way, using 1 μm wide nickel regions on a 2 μm pitch (Fig. 3.3b), exhibited periodic variations in contrast extending over the full length of the 65-μm-long NW. Analysis of the image showed that the average lengths of the Si and NiSi regions were both 1 μm, in good agreement with the width and pitch of nickel metal deposited on the NW during fabrication. TEM images of similar NiSi/SiNW heterostructures (Fig. 3.3c) showed a similar periodic contrast variation that was consistent with NiSi (dark) and Si (light) materials within the heterostructure. Detailed examination of NiSi/Si heterostructure by HRTEM (Fig. 3.3d) showed that the transformation yielded an atomically abrupt interfaces. The single crystalline nature of the NiSi/Si structures contrasts the polycrystalline structures obtained by templated-based electrodeposition, and moreover, represents ideal atomically-resolved structures for investigating fundamental electrical transport questions.

In subsequent work, Lin et al. [27] extended this work with the formation of PtSi/Si/PtSi NW heterostructures (Fig. 3.3e–g). The SiNW device with platinum contacts was fabricated on Si/Si_3N_4 substrate using e-beam lithography and e-beam evaporation (Fig. 3.3e). Then, the device was annealed at high temperature to allow platinum to diffuse into the SiNW and form partially (Fig. 3.3f) or fully silicidized PtSi NW (Fig. 3.3g). The phenomenon was attributed to the fact that many platinum atoms were dissolved into silicon through the contacts between SiNWs and Pt pads so that supersaturation was reached. Hence, nucleation and growth of platinum silicide occurred from both platinum pads.

3.3.4 p-n *Homojunctions*

A general scheme for realizing dopant modulation in the frame of metal nanocluster catalyzed NW synthesis involves varying the dopant reactant concentration in the vapor phase during growth. In this approach, it is essential to avoid radial overcoating during growth (Fig. 3.4a), since this can eliminate the desired electronic modulation in NW properties. To meet the desired synthetic goals, Yang et al. [28] carried out growth in H_2, which suppressed the decomposition of silane, and slowed the growth rate by uncatalyzed processes on the SiNW body. In addition, a local substrate heater was adopted to reduce reactant heating and possible homogeneous decomposition prior to delivery to the substrate and nanocluster catalyst. TEM studies of modulation-doped n^+-n-n^+ SiNWs (Fig. 3.4b), where n^+ and n represent the heavily and lightly doped n-type regions, respectively, showed that the NWs prepared in this way had uniform diameters for lengths of >10 μm. The diameters of the opposite ends of a representative n^+-n-n^+ SiNW were 17.4 and 17.1 nm, respectively. The 0.3-nm variation was on the order of a single atomic layer and

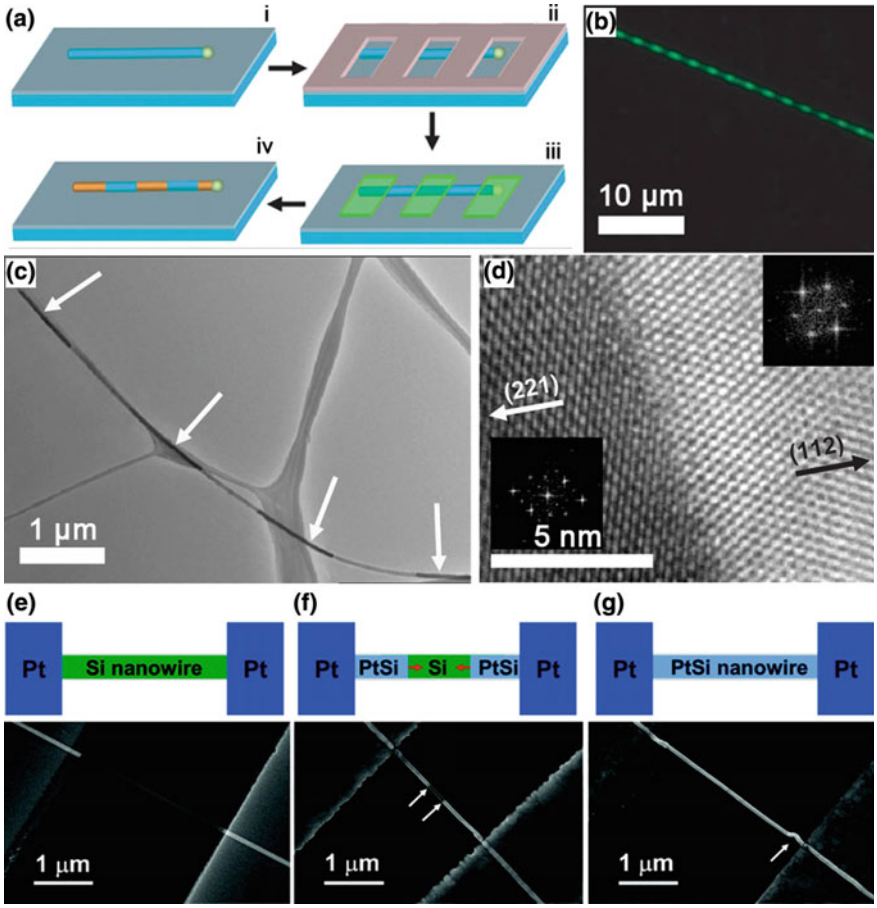

Fig. 3.3 **a** Fabrication of NiSi/SiNW heterostructures and superlattices: *i* SiNWs (*blue*) dispersed on a substrate are *ii* coated with photoresist (*grey*) and lithographically patterned, *iii* selectively coated with Ni and *iv* annealed to form NiSi NWs. **b** Dark field optical image of a single NiSi/SiNW heterostructure. The *bright green* segments correspond to silicon and the *dark* segments to NiSi. **c** TEM image of a NiSi/SiNW heterostructure. The *bright* segments of the NW correspond to silicon and the *dark* segments correspond to NiSi. **d** HRTEM image of the junction between NiSi and Si showing an atomically abrupt interface. Reproduced from [26]. Copyright 2004 Nature Publishing Group. **e**–**g** Schematic illustrations and corresponding SEM images depicting growth of a PtSi/Si/PtSi nanoheterostructure and PtSi NWs. **e** SiNW device with two Pt contact pads before reaction. **f** PtSi/Si/PtSi heterostructure obtained through partial silicidation of the SiNW. **g** PtSi NW after complete silicidation. Reproduced from [27]. Copyright 2008 American Chemical Society

showed that radial overcoating was effectively eliminated during growth of these modulation-doped structures. Representative scanning gate microscopy (SGM) data taken on modulation doped n^+-$(n$-$n^+)_N$ SiNWs with $N = 3$, 6 and 8 were shown in Fig. 3.4c–e. The pitch spacings in these dopant modulated structures, defined as the

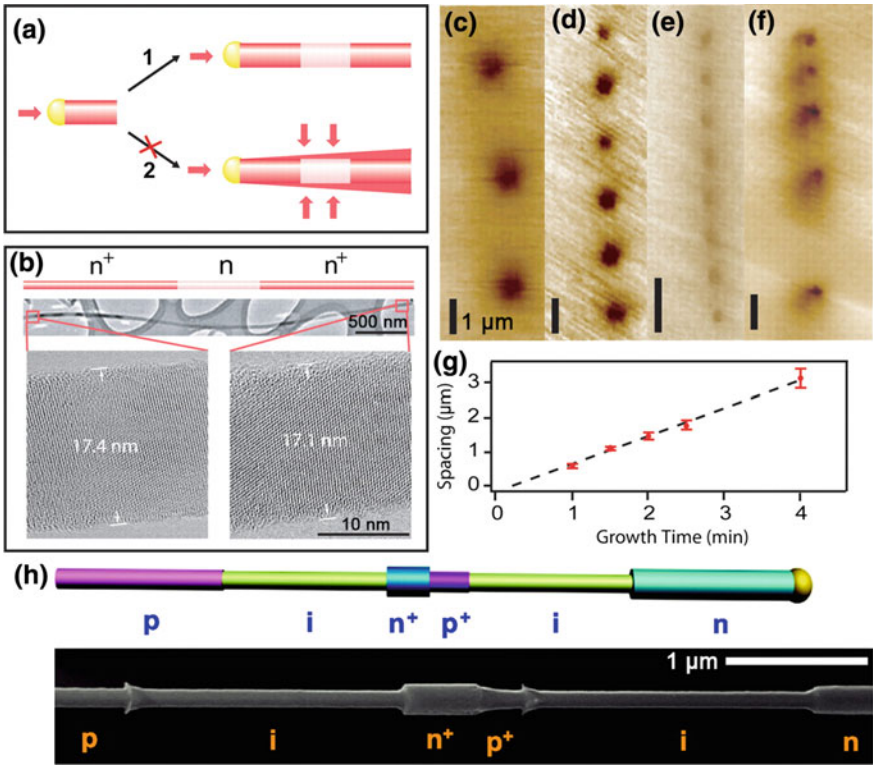

Fig. 3.4 **a** Schematic of the synthesis of modulation doped SiNW. Au colloid (*yellow*) catalyses growth of a heavily doped region (*red*) and lightly doped region (*pink*) NW superstructures. *1* Pure axial growth, resulting in dopant modulated NW super structure. *2* Axial and radial growth, resulting in a layer of homogenous overcoating (*red*) and a taped NW structure. **b** Schematic and TEM images of a representative n^+-n-n^+ modulation doped SiNW. **c**–**f** SGM images of n^+-$(n$-$n^+)_N$ NWs. **g** Repeat spacing versus growth time under fixed growth conditions. Reproduced from [28]. Copyright 2005 the American Association for the Advancement of Science. **h** Schematic and SEM image of a selectively etched tandem p-i-n^+-p^+-i-n SiNW. Reproduced from [29]. Copyright 2008 American Chemical Society

separation between two nearest *n* regions, were readily controlled by growth time, with the average values of 3.2 μm (Fig. 3.4c), 1.6 μm (Fig. 3.4d) and 0.8 μm (Fig. 3.4e), and could even be varied within a single NW (Fig. 3.4f). Detailed studies revealed that the pitch spacing was directly proportional to growth time (Fig. 3.4g).

In another study, the experimental realization of axial modulation-doped p-i-n and tandem p-i-n^+-p^+-i-n SiNWs was reported [29] (Fig. 3.4h). The heavily doped n^+ and p^+ regions were readily identifiable because of their positions in the tandem device, reduced degree of post growth wet chemical etching, and expected lengths

(~0.5 μm). These results confirm that the synthetic approach can yield the desired tandem junction sequence and allow precise control over the length of the doped regions.

3.3.5 *Ultrashort Morphology Features*

The formation of ultrashort NW structures could allow for superior and unconventional device performance. Cohen-Karni et al. [30] reported a new synthetic method that combines gold-nanocluster catalyzed VLS and VSS NW growth modes to produce synthetically encoded NW devices with ultra-sharp (<5 nm) *n*-type highly doped (n^{++}) to lightly doped (*n*) transitions along the NW growth direction. The abrupt *n*-Si/n^{++}-Si junctions were made possible due to slow growth rates of the VSS mechanism, which were at least 10-100 times lower than for VLS grown NWs.

Later, Christesen et al. [31] reported a bottom-up method to break the conventional "wire" symmetry and synthetically encode a high-resolution array of arbitrary shapes, including nanorods, sinusoids, bowties, tapers, nanogaps, and gratings, along the NW growth axis. Rapid modulation of phosphorus doping combined with selective wet-chemical etching enabled morphological features as small as 10 nm to be patterned over wires more than 50 μm in length. In their experiments, SiNWs were grown by a VLS mechanism in a home-built, hot-wall CVD system using Au nanoparticles as catalysts, SiH_4 as the source of Si, and H_2 as the carrier gas. As illustrated in Fig. 3.5a, an additional flow of phosphine (PH_3) was rapidly modulated during growth to encode varying levels of P, an *n*-type substitution dopant with high solubility in Si. The etching rate of doped Si with aqueous KOH solution was decreased with higher dopant concentration. NWs with six intrinsic segments encoded along the axis for increasingly short time scales were obtained (Fig. 3.5b). The authors also used other complex doping profiles to encode the range of morphological features shown in SEM images in Fig. 3.5c. These structures included periodic (images 1–4) or nonperiodic (image 5) gratings, nanogaps with gap sizes as small as 10 nm (images 6–7), suspended nanorods (image 8), and sinusoidal profiles (images 9–10).

3.4 Radial/Coaxial Modulated Structures

During VLS growth of semiconductor NWs, two compositionally-distinct material surfaces are exposed to the vapor: that of the metal-semiconductor liquid nanocluster catalyst and that of the solid semiconductor (Fig. 3.6a). If vapor decomposition/adsorption continues exclusively at the surface of the metal-semiconductor catalyst, crystalline growth of the new semiconductor will continue, inducing axial growth (Fig. 3.6b). On the other hand, if the new

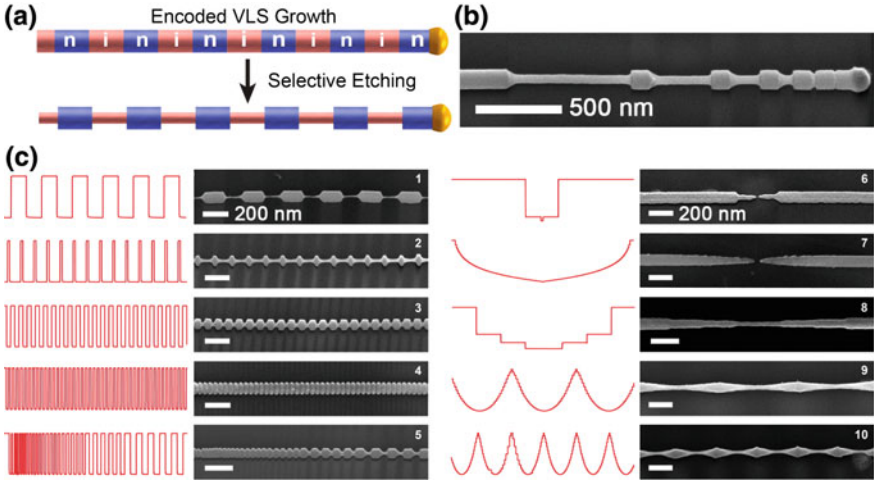

Fig. 3.5 **a** Schematic illustration of NW with heavily doped *n*-type (*n*) and undoped intrinsic (*i*) segments. **b** SEM image of a NW grating encoded (from *left* to *right*) with sequential intrinsic segments for 200, 100, 50, 25, 10, and 5 s. **c** SEM images and phosphine flow profiles for the synthesis of SiNWs with complex morphology. The measured phosphine flow profile used to encode the morphology of each segment is depicted in *red* to the *left* of each SEM image. Reproduced from [31]. Copyright 2013 American Chemical Society

vapor/reactant does not decompose/adsorb exclusively at the catalyst surface, but at the surface of the semiconductor NW, a shell of material will grow on the original NW surface (Fig. 3.6c). Subsequent introduction of different reactants and/or dopants can then be used to produce multiple shell structures of nearly arbitrary composition (Fig. 3.6d), although the epitaxial growth of these shells requires consideration of the lattice structures [32]. The interfacial kinetics, controlled by varying the pressure, flow rate, temperature, reactant species and background gases, is therefore necessary to control the dominant growth mode. In the previous section, we have discussed the formation of axial NW superlattices, which can be induced by repeated changing of reactants in a regime favoring axial growth. In this section, core-multi-shelled radial structures formed by changing reactants in a radial-growth regime will be introduced.

3.4.1 Semiconductor Radial Structures

One of the first reports of core/shell NW heterostructures was reported by Lauhon et al. [32] by using a nanocluster catalyzed CVD approach to grow NW core/shell homo- and heterostructures from Si and Ge, with different dopant concentration and types including *i*-Si/*p*-Si, Si/Ge and Ge/Si core-shell NWs. TEM images of the *i*-Si/*p*-Si product showed a uniform core-shell structure consisting of a crystalline Si

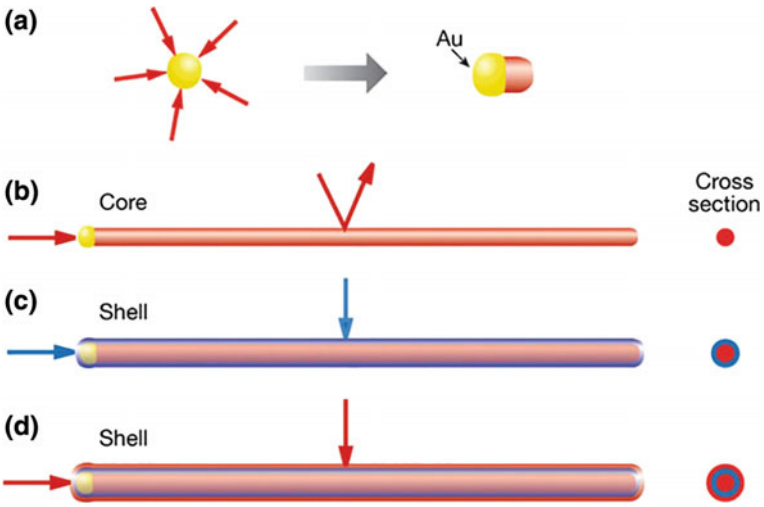

Fig. 3.6 **a** Gaseous reactants (*red*) catalytically decompose on the surface of a gold nanocluster leading to nucleation and directed NW growth. **b** One-dimensional growth is maintained as reactant decomposition on the gold catalyst is strongly preferred. **c** Synthetic conditions are altered to induce homogeneous reactant decomposition on the NW surface, leading to a thin, uniform shell (*blue*). **d** Multiple shells are grown by repeated modulation of reactants. Reproduced from [32]. Copyright 2002 Nature Publishing Group

core and an amorphous Si shell (Fig. 3.7a). In contrast, TEM images of the *i*-Si/SiO_x/*p*-Si core/shell/shell structures showed a smooth and abrupt interface between the crystalline core and amorphous shell (Fig. 3.7b, c). These results demonstrated that the thin oxide layer disrupted homoepitaxial growth. Further TEM studies showed that oxidation inhibited crystallization of the shell under annealing conditions. The authors also explored the synthesis of Si/Ge core/multishell NW structures. Figure 3.7d shows the bright-field TEM images and elemental mapping of a core/shell structure that is consistent with Ge-core (dark) and Si-shell (light) structure. High-resolution TEM images and cross-sectional elemental mapping of both Si/Ge and Ge/Si core-shell NWs are displayed in Fig. 3.7e, f. Later, Qian et al. demonstrated the synthesis of core/multishell NWs with an *n*-GaN core, $In_xGa_{1-x}N$/GaN/*p*-AlGaN/*p*-GaN shells [33] and highly uniform $(InGaN/GaN)_n$ quantum wells [34]. In the latter case, cross-sectional STEM images of three distinct multi-quantum-well (MQW) NWs (Fig. 3.7g–i) showed structures with resolvable 3, 13, and 26 periods, quantum-well thicknesses of about 2.4, 3.0 and 1.5 nm and average GaN barrier thicknesses of about 40, 10 and 1 nm, respectively.

In 2013, Kempa et al. [35] demonstrated regioselective NW shell synthesis in studies of Ge and Si growth on faceted SiNW surfaces. Generally, the structures were realized by breaking the rotational symmetry of conventional radial shell growth (Fig. 3.7j, k). To explore more complex and opto-electronically active

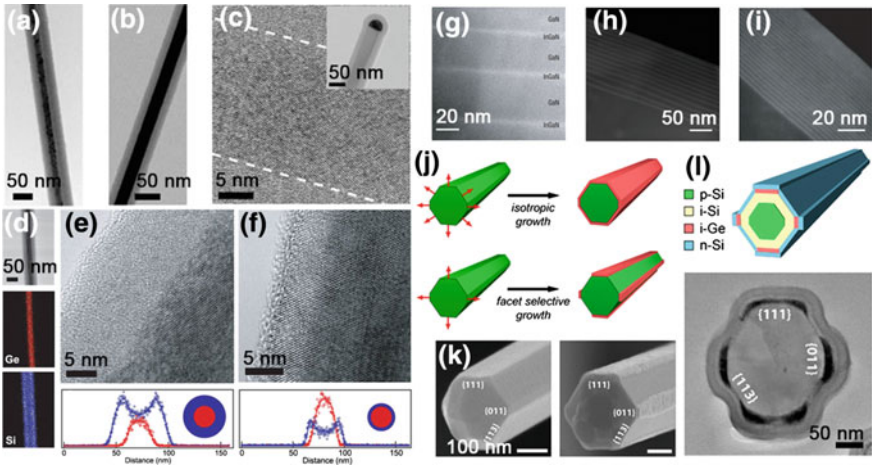

Fig. 3.7 **a** TEM image of an unannealed intrinsic silicon core and *p*-type silicon shell NW. **b**, **c** TEM images of an *i*-Si/SiO_x/*p*-Si NW. **d** Bright-field image and scanning TEM elemental maps of Ge (*red*) and Si (*blue*) concentrations of an unannealed Ge/Si core-shell NW. **e**, **f** HRTEM image and elemental mapping cross-section of an unannealed (**e**) and an annealed (**f**) Ge/Si core-shell NWs. Reproduced from [32]. Copyright 2002 Nature Publishing Group. **g–i** Dark-field cross-sectional STEM images MQW NW structures. Reproduced from [34]. Copyright 2008 Nature Publishing Group. **j** Schematics depicting isotropic versus anisotropic growth of Ge (*red*) on a faceted Si template (*green*). **k** SEM of a faceted Si template (*left*) and of a nanostructure (*right*) after selective deposition of Ge (*lighter contrast*) on Si. **l** Schematic and bright-field TEM image of the cross section of a complex nanostructure with Ge regions selectively embedded within a *p-i-n* junction. Reproduced from [35]. Copyright 2013 American Chemical Society

nanostructures, the authors encapsulated nanoscale Ge regions within a Si *p-n* interface. The targeted architecture included a faceted template with *p*-type and intrinsic Si shells, facet selectively grown Ge, and finally a conformal shell of *n*-type Si (Fig. 3.7l). Bright-field TEM image of the nanostructure cross sections verified that Ge was selectively embedded within the nanostructure while preserving the radial Si *p-n* junction. Later, the same group [36] demonstrated facet-selective growth of CdS on SiNWs. The crystalline CdS is grown epitaxially on the {111} and {110} surface facets of the SiNWs but the {113} facets remain bare. Further analysis of CdS on SiNWs grown at higher deposition rates to yield a conformal shell reveals a thin oxide layer on the Si{113} facet. This observation and control experiments suggest that facet-selective growth is enabled by the preferential formation of an oxide, which prevents subsequent shell growth on the Si{113} NW facets.

The Plateau–Rayleigh instability was first proposed in the mid-1800s to describe how a column of water breaks apart into droplets to lower its surface tension. This instability was later generalized to account for the constant volume rearrangement of various one-dimensional liquid and solid materials. The Lieber group [37] reported a growth phenomenon that is unique to one-dimensional materials and

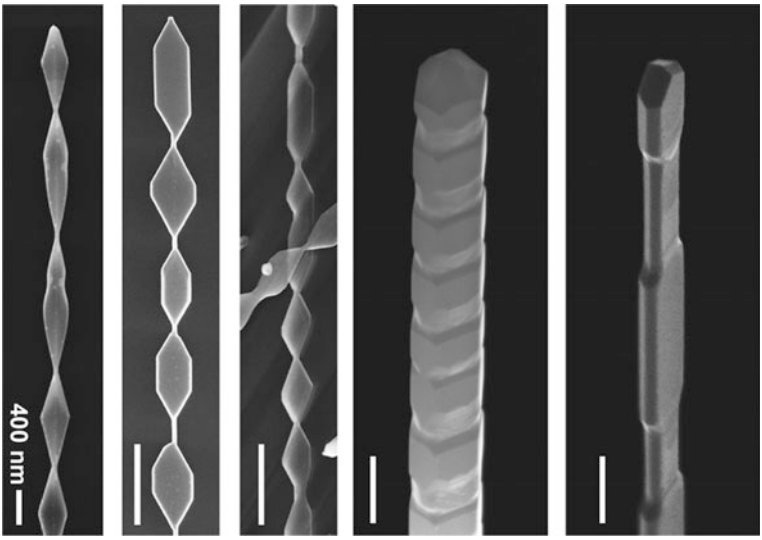

Fig. 3.8 SEM images of Si periodic shells deposited on SiNW cores achieved by Plateau–Rayleigh growth. Reproduced from [37]. Copyright 2015 Nature Publishing Group

exploited the underlying physics of the Plateau–Rayleigh instability. This phenomenon can be used to grow periodic shells on one-dimensional substrates. Specifically, the authors showed that for certain conditions, depositing Si onto uniform-diameter Si cores, Ge onto Ge cores and Ge onto Si cores can generate diameter-modulated core–shell NWs. Rational control of deposition conditions enables tuning of distinct morphological features, including diameter-modulation periodicity and amplitude and cross sectional anisotropy. The results suggested that surface energy reductions drive the formation of periodic shells, and that variation in kinetic terms and crystal facet energetics provide the means for tunability (Fig. 3.8).

3.4.2 Coaxial Modulated Structures

In addition to semiconductor radial structures, coaxial modulated NW structures have also been demonstrated [38–40]. For example, Tian et al. [39] reported the realization of *p-i-n* coaxial SiNWs (Fig. 3.9a). In this work, SiNW *p*-cores were first synthesized by the nanocluster catalyzed VLS method. Si shells were then deposited at a higher temperature and lower pressure than for *p*-core growth (Fig. 3.9a, right panel) to inhibit axial elongation of the SiNW core during the shell deposition, where phosphine was used as the *n*-type dopant in the outer shell. SEM images of a typical *p-i-n* SiNW (Fig. 3.9b) show the single crystalline NW core expected for SiNWs obtained by the VLS method and polycrystalline shells with a

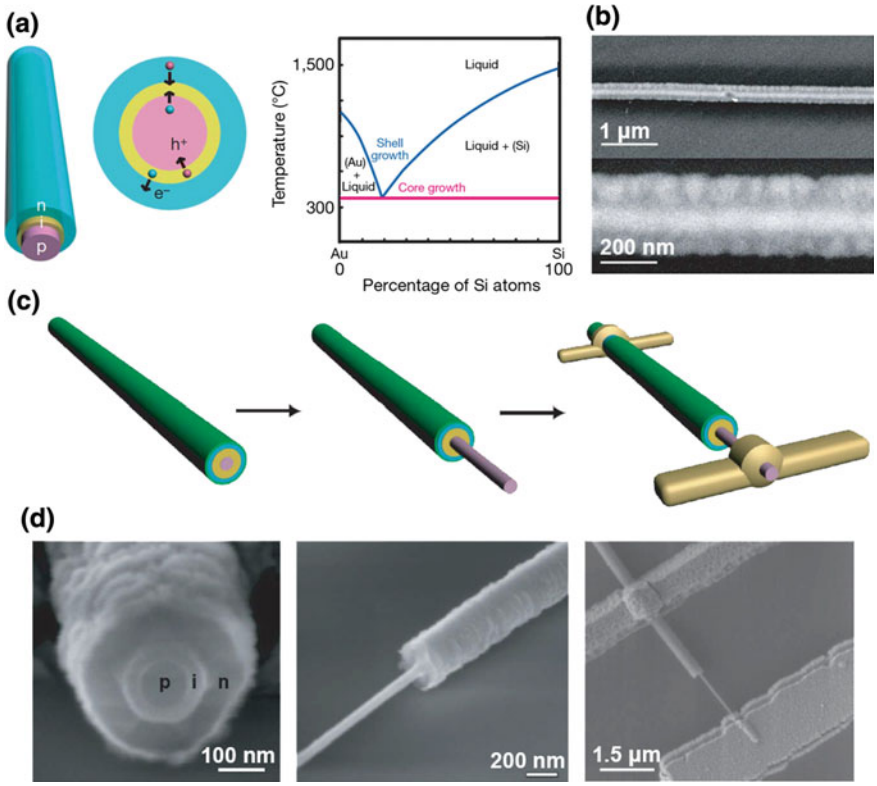

Fig. 3.9 **a** Illustrations of the core/shell SiNW structure. The phase diagram of Au–Si alloy on the right panel illustrates that the core is grown by means of the VLS mechanism, whereas the shells are deposited at higher temperature and lower pressure to inhibit further NW axial elongation. **b** SEM images of the *p*-*i*-*n* coaxial SiNW. **c**, **d** Schematics and corresponding SEM images of selective etching to expose the *p*-core and deposition of metal contacts on the *p*-core and *n*-shell. Reproduced from [39]. Copyright 2007 Nature Publishing Group

grain size on the order of 30–80 nm. To characterize electrical transport through the *p*-*i*-*n* coaxial SiNWs, the authors fabricated metal contacts selectively to the inner *p*-core and outer *n*-shell (Fig. 3.9c, d), where NWs were etched selectively using KOH solution to expose the *p*-core in a lithographically defined region, enabling the deposition of metal contacts in a following lithography step.

3.5 Branched/Tree-Like Structures

There have recently been substantial interests in production of branched/tree-like NW structures. The higher degree of complexity in such structures increases the potential for NW applications by increasing the number of connection points and

providing a means for parallel connectivity and interconnection of functional elements. In this section, we introduce various methodologies and mechanisms developed for the synthesis of branched structures, ranging from sequential catalyst-assisted growth, solution growth on existing NWs, phase transition induced branching, one-step self-catalytic growth and screw dislocation driven growth. The growth of these branched NWs have been reviewed [41].

3.5.1 Sequential Catalyst-Assisted Growth

Similar to the VLS growth of 1D semiconductor NWs, growth of branched or even hyperbranched NWs can be carried out in a controlled manner by introducing new nanocluster catalysts onto the primary NW surfaces. As a result, many efforts to grow these complex structures have been focused on the sequential catalyst-assisted method [42–46]. Typically, the process of synthesizing hyperbranched NWs involves sequential steps, as shown in Fig. 3.10a [42]: First, a NW backbone of specific diameter and composition is prepared by nanocluster-mediated VLS growth. Second, nanocluster catalysts of defined diameter are deposited on the backbone, and then the first-order branches are grown by the VLS process. Third, the branch growth steps can be repeated one or more times to yield higher order or hyperbranched NW structures. This method allows good control of the density of branches by adjusting the amount of Au particles deposited on the primary NW trunks, and length of the branches by the growth time. Figure 3.10b–e show representative SEM images of branched SiNW structures prepared by using increasing concentrations of gold nanoclusters during the deposition process. Furthermore, this approach can be extended to produce more complex NW architectures by a three-step growth procedure, in which 40, 20, and 10 nm gold nanoclusters were used to catalyze the VLS growth of the SiNWs comprising the backbone, first generation, and second generation branches, respectively (Fig. 3.10f). Simultaneously, the Samuelson group [43] also fabricated ordered arrays of GaP nanotrees (Fig. 3.10g) using a similar method. Au aerosol particles were deposited onto the primary vertically-aligned GaP NW stems for the subsequent VLS growth of GaP branches.

Compared with the above homobranched NWs, there had been much less reports on heteroepitaxial growth of branches based on sequential catalyst-assisted method. The heterobranch growth is more challenging, as the solubility of dissimilar materials in the same metal catalyst are generally different, which requires different growth temperature and partial pressure. In addition, possible crystal phase change and lattice mismatching are also need to be considered and resolved. The reported successful growths include CdS nanobranches on ZnS backbone NWs [47, 48], GaAs, GaP and Ge nanobranches on SiNWs [49], and CdSe branches on ZnSe NWs based on a sequential growth [50]. For example, Jiang et al. [49] reported the

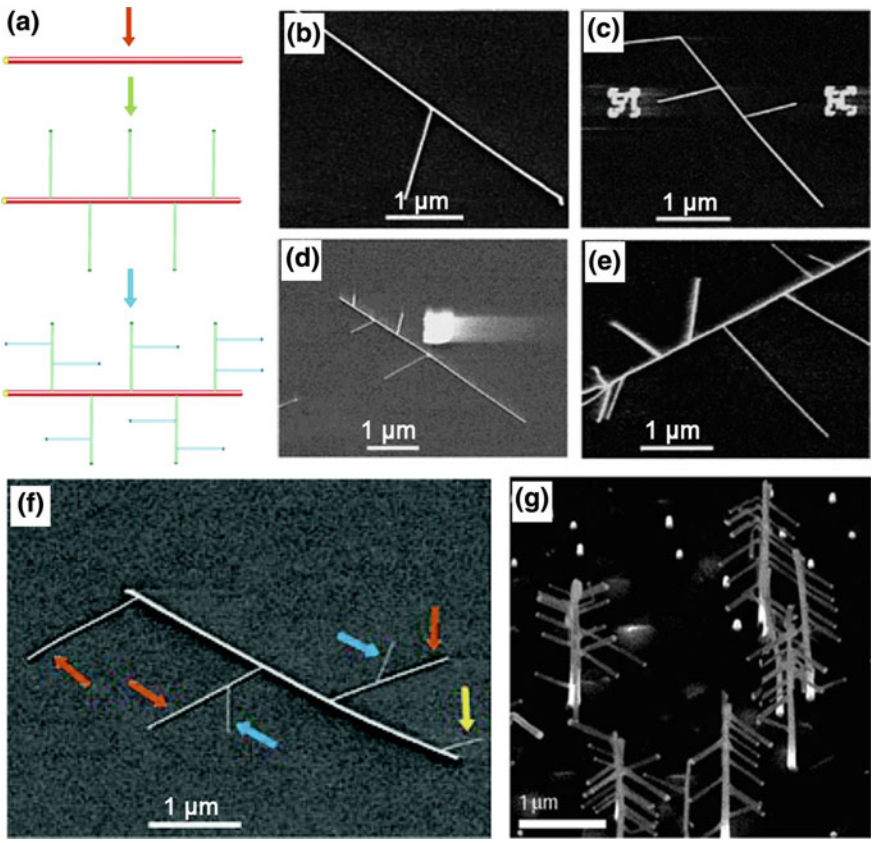

Fig. 3.10 **a** Schematic illustrating the multistep syntheses of branched and hyperbranched NW structures. **b–e** Branched SiNW structures prepared following deposition of gold nanoclusters from **b** 1:20, **c** 1:8, **d** 1:3, and **e** 1:1 diluted stock solutions and subsequent growth. **f** SEM image of a hyperbranched SiNW structure. The first-generation and second-generation branches are indicated by *orange* and *blue arrows*, respectively. *Yellow arrow* indicates a 10 nm SiNW (from second generation growth) grown from the backbone. Reproduced from [42]. Copyright 2004 American Chemical Society. **g** Ordered array of GaP nanotrees. Reproduced from [43]. Copyright 2004 Nature Publishing Group (Color figure online)

rational synthesis of branched NW structures, including group IV, III–V, and II–VI, with metal branches selectively grown on core or core-shell NW backbones. The composition, morphology and doping of core (core/shell) NWs and branched NWs were well controlled during the synthesis.

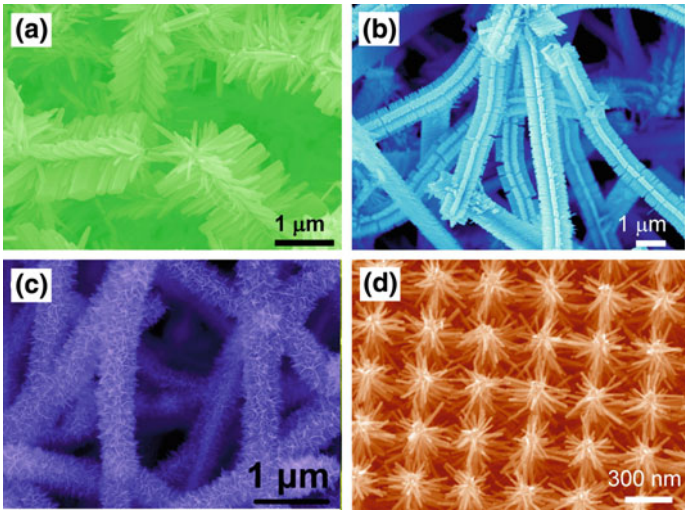

Fig. 3.11 Branched NWs with different material combinations prepared by solution growth on preformed NW backbones: **a** SnO_2/ZnO. Reproduced from [51]. Copyright 2009 American Chemical Society. **b** SnO_2/Fe_2O_3. Reproduced from [52]. Copyright 2011 John Wiley and Sons. **c** SnO_2/MnO_2. Reproduced from [53]. Copyright 2011 John Wiley and Sons. **d** Si/ZnO. Reproduced from [54]. Copyright 2010 American Chemical Society

3.5.2 Solution Growth on Existing Nanowires

Solution methods, including hydrothermal, solvothermal, chemical bath deposition and electrodeposition, can be applied to produce hierarchically branched NWs using pre-formed NWs as the growth substrate. Various types of 3D branched metal oxide NW heterostructures have been realized by combining VLS growth for the backbone NWs with the subsequent solution growth of branches [51–53]. VLS-grown SnO_2 NWs are very stable and are ideal candidates for the backbones of SnO_2/ZnO, SnO_2/Fe_2O_3 and SnO_2/MnO_2 branched NWs (Fig. 3.11a–c). Further, this method has also been extended to fabricate Si/ZnO forest-like arrays by hydrothermal growth of ZnO nanorods on lithographic-prepared Si nanopillars [54] (Fig. 3.11d).

3.5.3 Phase Transition Induced Branching

The Alivisatos group [55–58] introduced a phase transition induced branching method, through which branched NWs can be fabricated without the addition of branching catalyst. The concept underlying their work rests on controlling the relative stability and growth of two different crystal phases. Generally, these

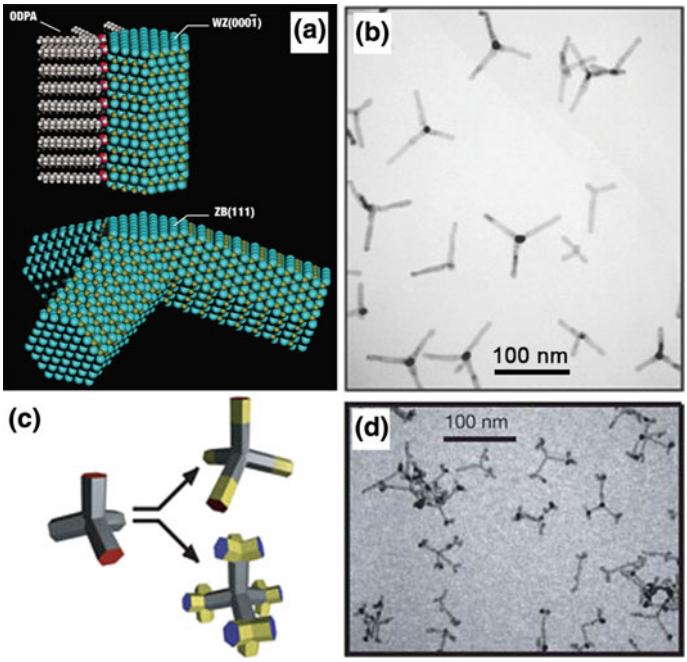

Fig. 3.12 **a** Proposed model of a CdTe tetrapod. **b** TEM images of the CdTe tetrapods. Reproduced from [56]. Copyright 2003 Nature Publishing Group. **c**, **d** Branched tetrapods resulted from nucleation of CdTe zinc blende branch points on the end of each arm. Reproduced from [57]. Copyright 2004 Nature Publishing Group

materials are limited to those that can crystallize in either wurtzite (WZ) or zinc blende (ZB) close-pack crystal structure or even mixed polytype under specific conditions. In CdTe [56] and other tetrahedrally bonded compound semiconductors, cubic and hexagonal crystal phases are often sufficiently close in energy such that both can be accessed by simply varying the reaction conditions. Following initial nucleation of cubic nanocrystallites, it was shown that four hexagonal arms can be selectively grown in high yield from the tetrahedral cubic nuclei by using organic surfactants to inhibit growth at the sides of the arms but not at their ends, thereby resulting in selective elongation. Figure 3.12a, b display the model of a CdTe tetrapod and TEM image of such crystallographic phase change-induced CdTe nanotetrapod. In a later report, the authors demonstrated that branched and linear junctions can be created not just at nucleation, but at any point during the growth of heterostructures [57]. As a proof of concept, they obtained branched NWs with CdSe in the first and CdTe in the second generation (Fig. 3.12c, d).

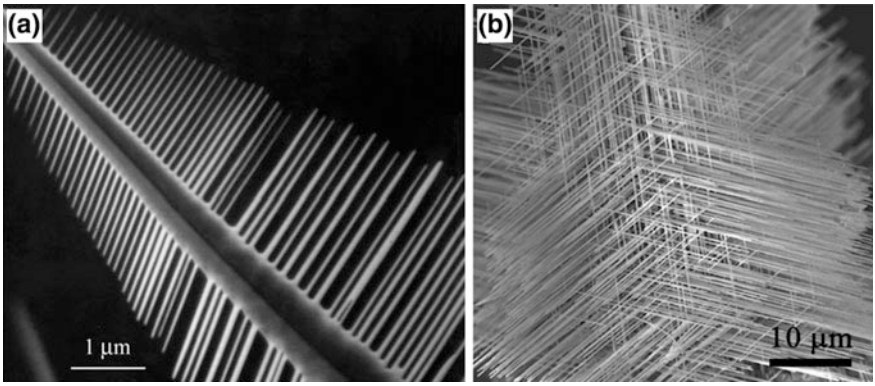

Fig. 3.13 **a** SEM image of comb structures made of ZnO NWs. Reproduced from [59]. Copyright 2003 American Chemical Society. **b** SEM image PbTe branched NWs. Reproduced from [60]. Copyright 2007 John Wiley and Sons

3.5.4 One-Step Self-catalytic Growth

In contrast to the sequential multi-step nanocluster catalyst deposition and growth, self-catalyzed growth allows preparation of 3D branched and even hyperbranched NWs in a single step [59–62]. Wurtzite crystals like ZnO and ZnS often exhibit a branched nanostructure. For example, Yan et al. [59] used the chemical vapor transport (CVT) method to fabricate highly ordered 1D microscale ZnO arrays that resembled comb structures (Fig. 3.13a). The individual NWs had uniform diameters ranging from 10 to 300 nm, and were evenly spaced on a stem with a regular periodicity of 0.1–2 μm. In another report, the same group [60] demonstrated CVT synthesis of arrays of PbS, PbSe, and PbTe NWs. As shown in Fig. 3.13b, the NW arrays were consisted of a central cube with NWs grown perpendicularly from each of the six faces.

3.5.5 Screw Dislocation Driven Growth

It has been suggested that the screw component of an axial dislocation can provide the self-perpetuating steps necessary to enable one-dimensional crystal growth without a nanocluster metal catalyst used in the VLS growth of NWs. In 2008, two groups reported NWs with rotating tree morphology made of PbS [63] and PbSe [64], respectively. In the former case, the authors observed pine tree-like NWs of PbS (Fig. 3.14) through CVD reactions [63]. These trees had trunks that are up to hundreds of micrometers in length and branches typically tens of micrometers long.

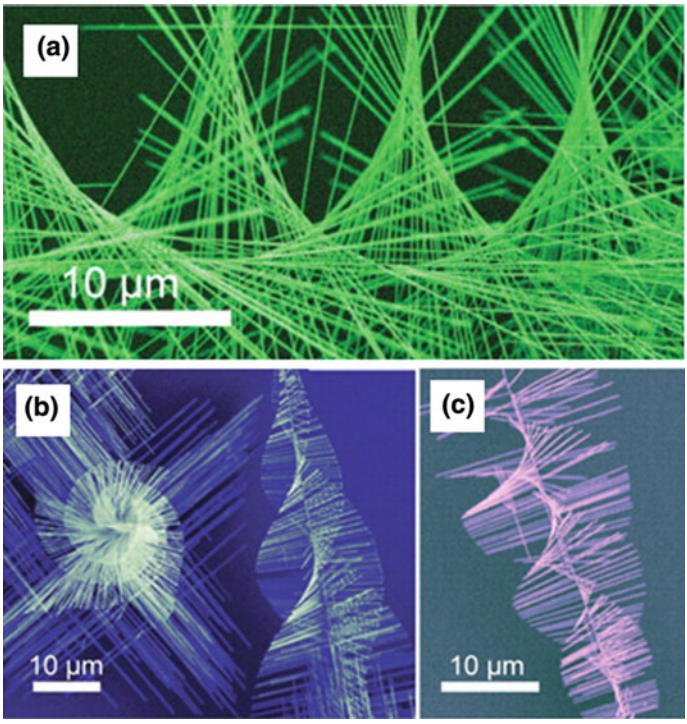

Fig. 3.14 High-magnification views of trees highlighting the twisting (Eshelby twist) of the central trunk and helical rotating branches. Reproduced from [63]. Copyright 2008 the American Association for the Advancement of Science

Individual wires grew consistently along the ⟨100⟩ crystallographic directions and their diameters ranged from 40 to 350 nm. Closer examination of these nanostructures revealed that each tree had four sets of epitaxial branches that were perpendicular to the trunk, and rotated around the trunk in a helical staircase fashion.

All dislocations create strain (and hence stress) within an otherwise perfect crystalline lattice. Using elasticity theory, it was shown that in a finite cylindrical rod containing an axial screw dislocation at the center, the stress field created by the dislocation exerts a torque at the free ends of the rod, resulting in a twist of the rod along the axial direction [63, 64]. The authors also carried out detailed examination of the formation mechanisms and kinetics of spontaneous NW and nanotube growth driven by screw dislocations [65, 66].

3.6 Kinked Structures

In this section, we will introduce methods to fabricate kinked NWs, which have unique 2 and 3D topologies defined by the kinks. Two basic classes of growth methods will be discussed, including the undersaturation/supersaturation-induced and confinement-guided kinking methods.

3.6.1 Undersaturation/Supersaturation-Induced Kinking

The Lieber group [67] developed a "nanotectonic" approach that provides iterative control over the nucleation and growth of NWs, and used it to grow kinked or zigzag NWs, in which the straight sections (secondary building unit, SBU) were separated by triangular joints (Fig. 3.15a). The SBU formation involves three main steps during nanocluster catalyzed growth (Fig. 3.15b): (1) axial growth of one-dimensional NW arm segments, (2) purging of gaseous reactants to suspend NW elongation, and (3) re-supersaturation and nucleation of NW growth following

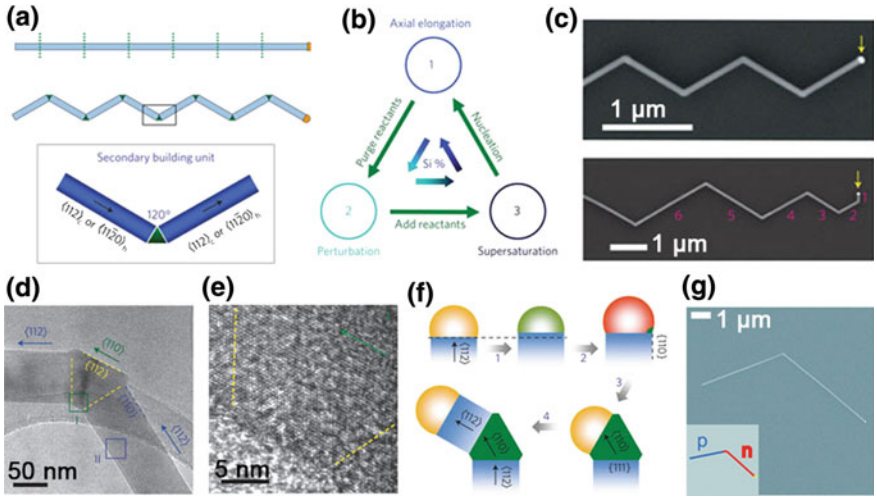

Fig. 3.15 **a** Schematic of a coherently kinked NW and the SBU, which contains two arms (*blue*) and one joint (*green*). **b** Cycle for the introduction of an SBU by stepwise synthesis. **c** SEM image of a kinked 2D SiNWs with equal (*upper panel*) and decreasing (*lower panel*) arm segment lengths. **d** TEM image of a single kink. **e** Lattice-resolved TEM images from regions *I* and *II* in (**d**). **f** Schematic illustrating the key stages of kink formation. *Arrows 1–4* denote purge, re-introduction of reactant, joint growth and subsequent arm growth, respectively. Reproduced from [67]. Copyright 2009 Nature Publishing Group. **g** Representative SEM image of a kinked *p-n* SiNW with 120° tip angle. Inset: Schematic of a kinked *p-n* NW with 120° tip angle. The *blue* and *red lines* designate the *p*-doped and *n*-doped arms, respectively. Reproduced from [68]. Copyright 2012 American Chemical Society

re-introduction of reactants. As illustrated for the case of silicon, the concentration of silicon-reactant dissolved in the nanocluster catalyst drops during purging and then reaches a maximum upon supersaturation. Repeating this cycle allows linking a number of SBUs, thus generating a two-dimensional chain structure (Fig. 3.15c). TEM images of a single kink further illustrate key SBU features (Fig. 3.15d, e). The above studies suggest that the kink formation can be qualitatively explained by the proposed stepwise model (Fig. 3.15f). In step 1, the reactant concentration drops in the supersaturated catalyst during the purge, and if the concentration is reduced sufficiently, elongation will cease. When reactant is re-introduced in step 2, the catalyst becomes supersaturated again and undergoes heterogeneous nucleation and growth. In step 3, growth proceeds with preservation of the most stable facets, implying that the heterogeneous nucleation should occur preferentially at the active edges of the three-phase boundary. In step 4, the kink is completed with a transition to another direction, thus completing a single SBU with coherent arm growth directions. Using a similar method, the same group [68] designed nanoscale axial *p–n* junctions that were synthetically introduced at the joints of kinked SiNWs (Fig. 3.15g).

Furthermore, the sterero configuration, such as *cis*- or *trans*-, has been demonstrated for the controlled kink growth. For example, two or three *cis*-linked kinked units can yield angles of 60° or 0°, respectively [69] (Fig. 3.16a, top and middle).

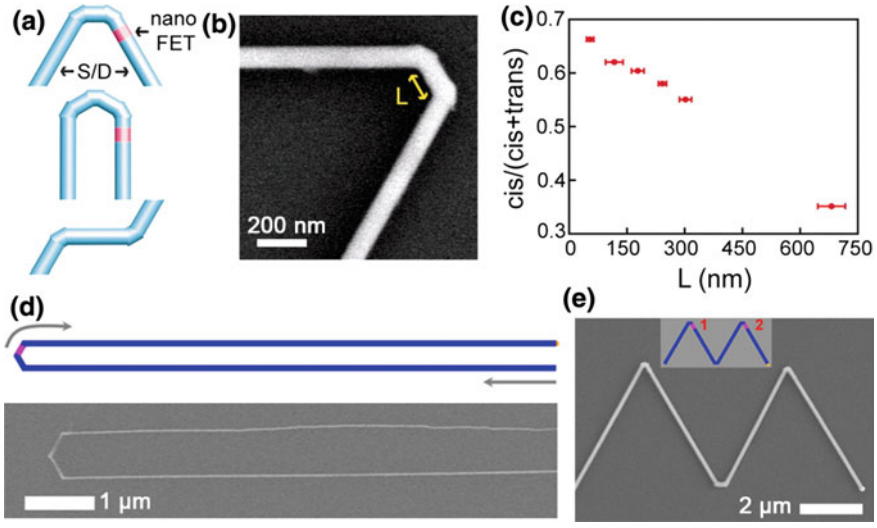

Fig. 3.16 **a** Schematics of 60° (*top*) and 0° (*middle*) multiply kinked NWs and *cis* (*top*) and *trans* (*bottom*) configurations in NW structures. **b** SEM image of a doubly kinked NW with a *cis* configuration. **c** *cis*/(*cis* + *trans*) versus *L* plot. Reproduced from [69]. Copyright 2010 the American Association for the Advancement of Science. **d** Schematic and SEM image of a U-shaped KNW with tip constructed from three 120° *cis*-linked kinks. **e** Schematic and SEM image of a W-shaped kinked NW. Reproduced from [70]. Copyright 2013 American Chemical Society

A representative SEM image of an 80-nm diameter, doubly kinked SiNW with an intervening segment length (L) of $\sim$160 nm between kink units (Fig. 3.16b) shows well-defined *cis*-linkage and an overall 60° tip angle. To investigate the ability of this method to synthesize this *cis*-linkage of kink structural units reproducibly, the authors analyzed the plot of *cis*/(*cis* + *trans*), as L was varied from $\sim$700 to 50 nm (Fig. 3.16c), showing that the *cis*-conformation becomes dominant as L decreases. In a follow-up report, Xu et al. [70] presented zero-degree kinked NW structures with U-shaped structures (Fig. 3.16d), as well as parallel kinked NWs with W-shaped structures (Fig. 3.16e).

3.6.2 *Confinement-Guided Kinking*

Pevzner et al. [71] demonstrated a confinement-guided NW growth method that allows unlimited control over geometry and location on a growth substrate. Following the VLS mechanism, semiconductor NWs down to a pitch lower than 50 nm of different compositions in a wide variety of two-dimensional shapes, such as any kinked (different turning angles), sinusoidal, linear, and spiral shapes, were demonstrated.

A schematic description of their method is shown in Fig. 3.17a. First, open trenches of a desired shape, size, number, density, orientation, and location are patterned by electron-beam lithography direct writing on a resist film on a Si wafer with a 600 nm thermal SiO_2 layer (i and ii). Trenches are then defined in the SiO_2 layer by chemical dry etching using RIE (iii). Second, titanium adhesion and gold layers of controlled thickness were deposited, where the latter functions as both the sacrificial material defining the enclosed channels and the catalyst for the following VLS-growth of Si, Ge and additional semiconductor NWs (iv). Subsequently, the resist film is lifted-off to reveal the gold lines on the substrate (v). Third, the openings of the tunnels are defined by photolithography (vi). Afterwards, a SiO_2 capping layer is deposited over the substrate by PECVD (vii). Finally, after the remaining resist is lifted-off (viii), the gold buried under the SiO_2 capping layer is controllably removed by wet etching with gold etchant to form the shape-controlled nanotunnels (ix). In order to retain a relatively short gold section at the end of the nanotunnels, which will sequentially serve as VLS catalysts for the NWs growth, the etching process is stopped by immersion of the substrate in deionized water. In the next process, Si or Ge NW growth is carried out in a hotwall or cold-wall CVD reactor via the VLS process (x). Finally, the removal of SiO_2 capping layer is done by chemical dry etching using RIE (xi). SEM images of synthesized NWs with a wide variety of 2D shapes are shown in Fig. 3.17b. These shapes include kinked Si and Ge NW structures with different turning angles of between 80 and 120° (i–iv), sinusoidal NWs (v–vii) with different periods and even more complex shapes like spirals (viii). The gold catalyst can be observed at the tip of the growing NWs (iii, v, viii), indicating that the growth proceeds via the VLS catalytic process throughout the entire synthesis.

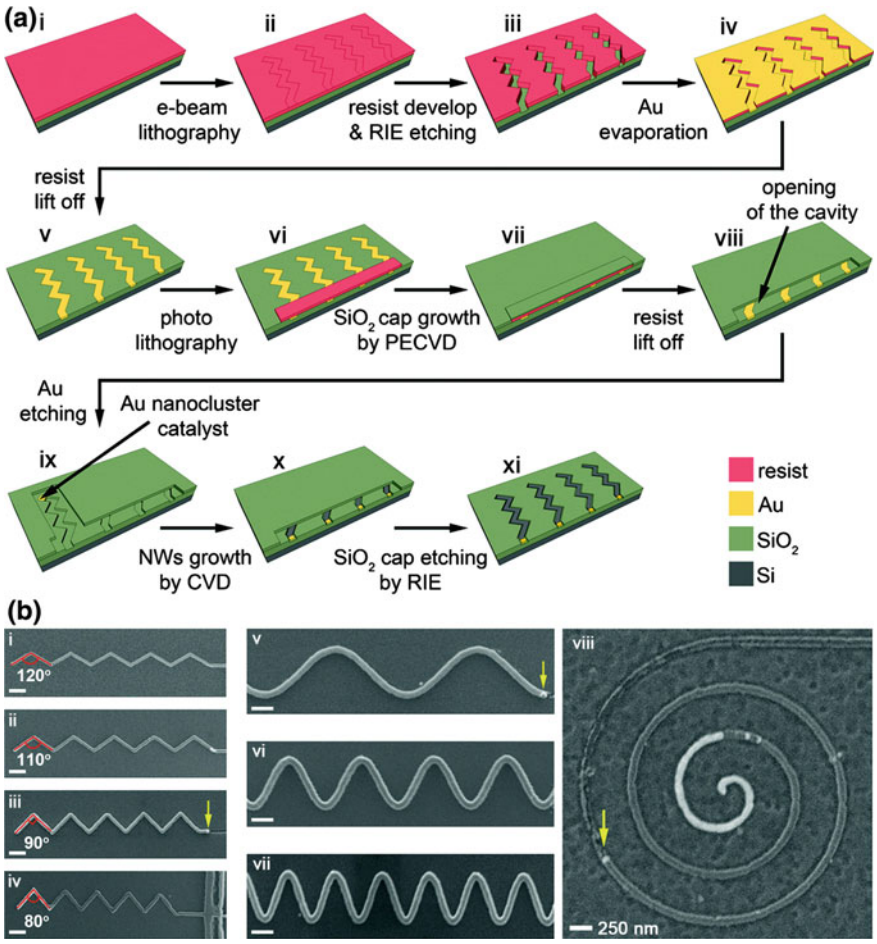

Fig. 3.17 **a** Schematic illustration of the shape-guided growth method. **b** SEM images of synthesized NWs with a wide variety of 2D shapes. *i–iv* Multiply kinked two-dimensional SiNWs with different turning angles from 120 to 80°. *v–vii* Sinusoidal shape two-dimensional SiNWs with different periods. *viii* SEM image of a two-dimensional spiral shape SiNW. The *yellow arrows* in *iii*, *v*, *viii* highlight the position of the nanocluster catalyst. Reproduced from [71]. Copyright 2012 American Chemical Society (Color figure online)

3.7 Future Directions and Challenges

The bottom-up paradigm of NW growth by the nanocluster catalyzed VLS method provides the unique opportunity for realizing rational control of physical dimensions and morphology, chemical composition, electronic structure and doping, which are the central elements that determine predictable device functions. The examples described in this chapter illustrate broadly how it is possible to achieve

increasing control over key parameters of the basic NW building blocks from homogeneous doped materials to increasingly complex axial, radial and branched heterostructures, as well as simultaneous axial and radial modulated, and topologically-defined structures.

Overall, the capability to design and synthesize diverse NW building blocks has enabled and will continue to drive the exploration of physical limits of nanostructures, investigating a broad range of scientific problems, discovering and/or uncovering new concepts, and ultimately driving technologies of the future. Nonetheless, in order to use these NW as building blocks to construct complex architectures and systems with novel functions, the capability of patterning NW assemblies into arrays over multiple length scales can be critical, and will be addressed in the next chapter.

References

1. C.M. Lieber, Semiconductor nanowires: a platform for nanoscience and nanotechnology. MRS Bull. **36**(12), 1052–1063 (2011)
2. M.S. Gudiksen, C.M. Lieber, Diameter-selective synthesis of semiconductor nanowires. J. Am. Chem. Soc. **122**(36), 8801–8802 (2000)
3. M.S. Gudiksen, J. Wang, C.M. Lieber, Synthetic control of the diameter and length of single crystal semiconductor nanowires. J. Phys. Chem. B **105**(19), 4062–4064 (2001)
4. Y. Cui, L.J. Lauhon, M.S. Gudiksen, J. Wang, C.M. Lieber, Diameter-controlled synthesis of single-crystal silicon nanowires. Appl. Phys. Lett. **78**(15), 2214–2216 (2001)
5. Y. Wu, Y. Cui, L. Huynh, C.J. Barrelet, D.C. Bell, C.M. Lieber, Controlled growth and structures of molecular-scale silicon nanowires. Nano Lett. **4**(3), 433–436 (2004)
6. W. Shi, H. Peng, Y. Zheng, N. Wang, N. Shang, Z. Pan, C. Lee, S. Lee, Synthesis of large areas of highly oriented, very long silicon nanowires. Adv. Mater. **12**(18), 1343–1345 (2000)
7. Y. Shi, Q. Hu, H. Araki, H. Suzuki, H. Gao, W. Yang, T. Noda, Long Si nanowires with millimeter-scale length by modified thermal evaporation from Si powder. Appl. Phys. A **80**(8), 1733–1736 (2005)
8. W.I. Park, G. Zheng, X. Jiang, B. Tian, C.M. Lieber, Controlled synthesis of millimeter-long silicon nanowires with uniform electronic properties. Nano Lett. **8**(9), 3004–3009 (2008)
9. F. Patolsky, G. Zheng, C.M. Lieber, Fabrication of silicon nanowire devices for ultrasensitive, label-free, real-time detection of biological and chemical species. Nat. Protoc. **1**(4), 1711–1724 (2006)
10. G. Zheng, W. Lu, S. Jin, C.M. Lieber, Synthesis and fabrication of high-performance n-type silicon nanowire transistors. Adv. Mater. **16**(21), 1890–1893 (2004)
11. J. Kikkawa, Y. Ohno, S. Takeda, Growth rate of silicon nanowires. Appl. Phys. Lett. **86**(12), 123109 (2005)
12. M. Masi, C. Cavallotti; S. Carrà, Gas phase and surface kinetics of silicon chemical vapor deposition from silane and chlorosilanes, in *Silicon-Based Materials and Devices*, ed. by M. Tomozawa, H. Nalwa (Academic Press, San Diego, 2001)
13. Y. Cui, X. Duan, J. Hu, C.M. Lieber, Doping and electrical transport in silicon nanowires. J. Phys. Chem. B **104**(22), 5213–5216 (2000)
14. L. Lauhon, M.S. Gudiksen, C.M. Lieber, Semiconductor nanowire heterostructures. Phil. Trans. R. Soc. Lond. A **2004**(362), 1247–1260 (1819)
15. R. Agarwal, Heterointerfaces in semiconductor nanowires. Small **4**(11), 1872–1893 (2008)

16. R.S. Wagner, Growth of whiskers by vapor-phase reactions, in *Whisker technology*, ed. by A.P. Levitt (Wiley, New York, 1970), pp. 15–119
17. K. Haraguchi, T. Katsuyama, K. Hiruma, K. Ogawa, GaAs p-n junction formed in quantum wire crystals. Appl. Phys. Lett. **60**(6), 745–747 (1992)
18. J. Hu, M. Ouyang, P. Yang, C.M. Lieber, Controlled growth and electrical properties of heterojunctions of carbon nanotubes and silicon nanowires. Nature **399**(6731), 48–51 (1999)
19. C.M. Lieber, Nanowire superlattices. Nano Lett. **2**(2), 81–82 (2002)
20. Y. Wu, R. Fan, P. Yang, Block-by-block growth of single-crystalline Si/SiGe superlattice nanowires. Nano Lett. **2**(2), 83–86 (2002)
21. M. Björk, B. Ohlsson, T. Sass, A. Persson, C. Thelander, M. Magnusson, K. Deppert, L. Wallenberg, L. Samuelson, One-dimensional steeplechase for electrons realized. Nano Lett. **2**(2), 87–89 (2002)
22. M. Björk, B. Ohlsson, T. Sass, A. Persson, C. Thelander, M. Magnusson, K. Deppert, L. Wallenberg, L. Samuelson, One-dimensional heterostructures in semiconductor nanowhiskers. Appl. Phys. Lett. **80**(6), 1058–1060 (2002)
23. M.T. Björk, C. Thelander, A.E. Hansen, L.E. Jensen, M.W. Larsson, L.R. Wallenberg, L. Samuelson, Few-electron quantum dots in nanowires. Nano Lett. **4**(9), 1621–1625 (2004)
24. M.S. Gudiksen, L.J. Lauhon, J. Wang, D.C. Smith, C.M. Lieber, Growth of nanowire superlattice structures for nanoscale photonics and electronics. Nature **415**(6872), 617–620 (2002)
25. D.J. Pena, J.K. Mbindyo, A.J. Carado, T.E. Mallouk, C.D. Keating, B. Razavi, T.S. Mayer, Template growth of photoconductive metal-CdSe-metal nanowires. J. Phys. Chem. B **106**(30), 7458–7462 (2002)
26. Y. Wu, J. Xiang, C. Yang, W. Lu, C.M. Lieber, Single-crystal metallic nanowires and metal/semiconductor nanowire heterostructures. Nature **430**(6995), 61–65 (2004)
27. Y.-C. Lin, K.-C. Lu, W.-W. Wu, J. Bai, L.J. Chen, K. Tu, Y. Huang, Single crystalline PtSi nanowires, PtSi/Si/PtSi nanowire heterostructures, and nanodevices. Nano Lett. **8**(3), 913–918 (2008)
28. C. Yang, Z. Zhong, C.M. Lieber, Encoding electronic properties by synthesis of axial modulation-doped silicon nanowires. Science **310**(5752), 1304–1307 (2005)
29. T.J. Kempa, B. Tian, D.R. Kim, J. Hu, X. Zheng, C.M. Lieber, Single and tandem axial p-i-n nanowire photovoltaic devices. Nano Lett. **8**(10), 3456–3460 (2008)
30. T. Cohen-Karni, D. Casanova, J.F. Cahoon, Q. Qing, D.C. Bell, C.M. Lieber, Synthetically encoded ultrashort-channel nanowire transistors for fast, pointlike cellular signal detection. Nano Lett. **12**(5), 2639–2644 (2012)
31. J.D. Christesen, C.W. Pinion, E.M. Grumstrup, J.M. Papanikolas, J.F. Cahoon, Synthetically encoding 10 nm morphology in silicon nanowires. Nano Lett. **13**(12), 6281–6286 (2013)
32. L.J. Lauhon, M.S. Gudiksen, D. Wang, C.M. Lieber, Epitaxial core–shell and core–multishell nanowire heterostructures. Nature **420**(6911), 57–61 (2002)
33. F. Qian, S. Gradecak, Y. Li, C.-Y. Wen, C.M. Lieber, Core/multishell nanowire heterostructures as multicolor, high-efficiency light-emitting diodes. Nano Lett. **5**(11), 2287–2291 (2005)
34. F. Qian, Y. Li, S. Gradečak, H.-G. Park, Y. Dong, Y. Ding, Z.L. Wang, C.M. Lieber, Multi-quantum-well nanowire heterostructures for wavelength-controlled lasers. Nat. Mater. **7**(9), 701–706 (2008)
35. T.J. Kempa, S.-K. Kim, R.W. Day, H.-G. Park, D.G. Nocera, C.M. Lieber, Facet-selective growth on nanowires yields multi-component nanostructures and photonic devices. J. Am. Chem. Soc. **135**(49), 18354–18357 (2013)
36. M.N. Mankin, R.W. Day, R. Gao, Y.-S. No, S.-K. Kim, A.A. McClelland, D.C. Bell, H.-G. Park, C.M. Lieber, Facet-selective epitaxy of compound semiconductors on faceted silicon nanowires. Nano Lett. **15**(7), 4776–4782 (2015)
37. R.W. Day, M.N. Mankin, R. Gao, Y.-S. No, S.-K. Kim, D.C. Bell, H.-G. Park, C.M. Lieber, Plateau-Rayleigh crystal growth of periodic shells on one-dimensional substrates. Nat. Nanotechnol. **10**(4), 345–352 (2015)

38. A.B. Greytak, L.J. Lauhon, M.S. Gudiksen, C.M. Lieber, Growth and transport properties of complementary germanium nanowire field-effect transistors. Appl. Phys. Lett. **84**(21), 4176–4178 (2004)
39. B. Tian, X. Zheng, T.J. Kempa, Y. Fang, N. Yu, G. Yu, J. Huang, C.M. Lieber, Coaxial silicon nanowires as solar cells and nanoelectronic power sources. Nature **449**(7164), 885–889 (2007)
40. D.C. Dillen, K. Kim, E.-S. Liu, E. Tutuc, Radial modulation doping in core-shell nanowires. Nat. Nanotechnol. **9**(2), 116–120 (2014)
41. C. Cheng, H.J. Fan, Branched nanowires: synthesis and energy applications. Nano Today **7**(4), 327–343 (2012)
42. D. Wang, F. Qian, C. Yang, Z. Zhong, C.M. Lieber, Rational growth of branched and hyperbranched nanowire structures. Nano Lett. **4**(5), 871–874 (2004)
43. K.A. Dick, K. Deppert, M.W. Larsson, T. Mårtensson, W. Seifert, L.R. Wallenberg, L. Samuelson, Synthesis of branched 'nanotrees' by controlled seeding of multiple branching events. Nat. Mater. **3**(6), 380–384 (2004)
44. Q. Wan, J. Huang, Z. Xie, T. Wang, E.N. Dattoli, W. Lu, Branched SnO_2 nanowires on metallic nanowire backbones for ethanol sensors application. Appl. Phys. Lett. **92**(10), 102101 (2008)
45. Q. Wan, E.N. Dattoli, W.Y. Fung, W. Guo, Y. Chen, X. Pan, W. Lu, High-performance transparent conducting oxide nanowires. Nano Lett. **6**(12), 2909–2915 (2006)
46. K.A. Dick, K. Deppert, L.S. Karlsson, M.W. Larsson, W. Seifert, L. Wallenberg, L. Samuelson, Directed growth of branched nanowire structures. MRS Bull. **32**(02), 127–133 (2007)
47. Y. Jung, D.-K. Ko, R. Agarwal, Synthesis and structural characterization of single-crystalline branched nanowire heterostructures. Nano Lett. **7**(2), 264–268 (2007)
48. W. Zhou, A. Pan, Y. Li, G. Dai, Q. Wan, Q. Zhang, B. Zou, Controllable fabrication of high-quality 6-fold symmetry-branched CdS nanostructures with ZnS nanowires as templates. J. Phys. Chem. C **112**(25), 9253–9260 (2008)
49. X. Jiang, B. Tian, J. Xiang, F. Qian, G. Zheng, H. Wang, L. Mai, C.M. Lieber, Rational growth of branched nanowire heterostructures with synthetically encoded properties and function. Proc. Natl. Acad. Sci. USA **108**(30), 12212–12216 (2011)
50. A. Dong, R. Tang, W.E. Buhro, Solution-based growth and structural characterization of homo-and heterobranched semiconductor nanowires. J. Am. Chem. Soc. **129**(40), 12254–12262 (2007)
51. C. Cheng, B. Liu, H. Yang, W. Zhou, L. Sun, R. Chen, S.F. Yu, J. Zhang, H. Gong, H. Sun, Hierarchical assembly of ZnO nanostructures on SnO_2 backbone nanowires: low-temperature hydrothermal preparation and optical properties. ACS Nano **3**(10), 3069–3076 (2009)
52. W. Zhou, C. Cheng, J. Liu, Y.Y. Tay, J. Jiang, X. Jia, J. Zhang, H. Gong, H.H. Hng, T. Yu, Epitaxial growth of branched α-Fe2O3/SnO2 nano-heterostructures with improved lithium-ion battery performance. Adv. Funct. Mater. **21**(13), 2439–2445 (2011)
53. J. Liu, J. Jiang, C. Cheng, H. Li, J. Zhang, H. Gong, H.J. Fan, Co_3O_4 nanowire@ MnO_2 ultrathin nanosheet core/shell arrays: a new class of high-performance pseudocapacitive materials. Adv. Mater. **23**(18), 2076–2081 (2011)
54. C. Cheng, B. Yan, S.M. Wong, X. Li, W. Zhou, T. Yu, Z. Shen, H. Yu, H.J. Fan, Fabrication and SERS performance of silver-nanoparticle-decorated Si/ZnO nanotrees in ordered arrays. ACS Appl. Mater. Interfaces **2**(7), 1824–1828 (2010)
55. L. Manna, E.C. Scher, A.P. Alivisatos, Synthesis of soluble and processable rod-, arrow-, teardrop-, and tetrapod-shaped CdSe nanocrystals. J. Am. Chem. Soc. **122**(51), 12700–12706 (2000)
56. L. Manna, D.J. Milliron, A. Meisel, E.C. Scher, A.P. Alivisatos, Controlled growth of tetrapod-branched inorganic nanocrystals. Nat. Mater. **2**(6), 382–385 (2003)
57. D.J. Milliron, S.M. Hughes, Y. Cui, L. Manna, J. Li, L.-W. Wang, A.P. Alivisatos, Colloidal nanocrystal heterostructures with linear and branched topology. Nature **430**(6996), 190–195 (2004)

58. D. Wang, C.M. Lieber, Inorganic materials: nanocrystals branch out. Nat. Mater. **2**(6), 355–356 (2003)
59. H. Yan, R. He, J. Johnson, M. Law, R.J. Saykally, P. Yang, Dendritic nanowire ultraviolet laser array. J. Am. Chem. Soc. **125**(16), 4728–4729 (2003)
60. M. Fardy, A.I. Hochbaum, J. Goldberger, M.M. Zhang, P. Yang, Synthesis and thermoelectrical characterization of lead chalcogenide nanowires. Adv. Mater. **19**(19), 3047–3051 (2007)
61. M.J. Bierman, Y.A. Lau, S. Jin, Hyperbranched PbS and PbSe nanowires and the effect of hydrogen gas on their synthesis. Nano Lett. **7**(9), 2907–2912 (2007)
62. R. Liu, Z.-A. Li, C. Zhang, X. Wang, M.A. Kamran, M. Farle, B. Zou, Single-step synthesis of monolithic comb-like CdS nanostructures with tunable waveguide properties. Nano Lett. **13** (6), 2997–3001 (2013)
63. M.J. Bierman, Y.A. Lau, A.V. Kvit, A.L. Schmitt, S. Jin, Dislocation-driven nanowire growth and Eshelby twist. Science **320**(5879), 1060–1063 (2008)
64. J. Zhu, H. Peng, A. Marshall, D. Barnett, W. Nix, Y. Cui, Formation of chiral branched nanowires by the Eshelby twist. Nat. Nanotechnol. **3**(8), 477–481 (2008)
65. S.A. Morin, M.J. Bierman, J. Tong, S. Jin, Mechanism and kinetics of spontaneous nanotube growth driven by screw dislocations. Science **328**(5977), 476–480 (2010)
66. S. Jin, M.J. Bierman, S.A. Morin, A new twist on nanowire formation: screw-dislocation-driven growth of nanowires and nanotubes. J. Phys. Chem. Lett. **1**(9), 1472–1480 (2010)
67. B. Tian, P. Xie, T.J. Kempa, D.C. Bell, C.M. Lieber, Single-crystalline kinked semiconductor nanowire superstructures. Nat. Nanotechnol. **4**(12), 824–829 (2009)
68. Z. Jiang, Q. Qing, P. Xie, R. Gao, C.M. Lieber, Kinked p–n junction nanowire probes for high spatial resolution sensing and intracellular recording. Nano Lett. **12**(3), 1711–1716 (2012)
69. B. Tian, T. Cohen-Karni, Q. Qing, X. Duan, P. Xie, C.M. Lieber, Three-dimensional, flexible nanoscale field-effect transistors as localized bioprobes. Science **329**(5993), 830–834 (2010)
70. L. Xu, Z. Jiang, Q. Qing, L. Mai, Q. Zhang, C.M. Lieber, Design and synthesis of diverse functional kinked nanowire structures for nanoelectronic bioprobes. Nano Lett. **13**(2), 746–751 (2013)
71. A. Pevzner, Y. Engel, R. Elnathan, A. Tsukernik, Z. Barkay, F. Patolsky, Confinement-guided shaping of semiconductor nanowires and nanoribbons: “writing with nanowires”. Nano Lett. **12**(1), 7–12 (2012)